JOURNAL OF MATERIALS SCIENCE 33 (1998) 4365–4374

# Effects of composition on microstructures of rapidly solidified Ni–Al alloys

TIANYI CHENG
*Metal Materials Section, Beijing Institute of Technology, P.O. Box 327, Beijing 100081, People's Republic of China*

W. LÖSER, M. LEONHARDT
*Institut für Festkörper- und Werkstofforschung Dresden, Institut für Metallische Werkstoffe, P.O. Box 27 00 16, D-01171 Dresden, Germany*
*E-mail: Loeser@ifw-dresden.de*

Microstructures of melt-spun Ni–Al alloys with compositions from 61–85 at % Ni were studied by means of transmission electron microscopy, X-ray diffraction analysis and optical microscopy. The microstructures of as-quenched ribbons exposed to cooling rates of the order of $10^6\,K\,s^{-1}$ reflect the transition from primary β-NiAl to γ-Ni solidification with increasing nickel content. In 70 at % Ni alloy ribbons, martensitic NiAl grains were detected near the wheel-side surface contrasting with anomalous and lamellar eutectic microstructure in the top part. Directly ordered $Ni_3Al$ grains with single (or large) antiphase domains (APDs) and a minor eutectic fraction were observed in 75 at % Ni alloy ribbons. Samples containing 80 at % Ni exhibit mainly single-phase $Ni_3Al$ grains with 10–20 nm sized APDs indicating sequential ordering. Weak $L1_2$ ordering was even detected in 85 at % Ni ribbons which displayed ordered antiphase zones of 1 nm size. Disordered γ-(Ni) films on grain boundaries can be discounted for 80 at % Ni ribbons, but occurred near the top of 85 at % Ni samples. The results are explained in terms of the reassessed Ni–Al phase diagram employing recent corrections near to the $Ni_3Al$ composition and new results on phase formation in undercooled Ni–Al melts. © *1998 Kluwer Academic Publishers*

## 1. Introduction

Much attention has been focused on the study of Ni–Al alloys because of several interesting intermetallic compounds formed in this alloy system [1]. Among these intermetallics, the $L1_2$ ordered $Ni_3Al(\gamma')$ phase and the B2 ordered NiAl (β) phase are most attractive because of potential applications as high-temperature structural materials [2–4]. This is closely related to their stable ordered structure both at room and elevated temperatures. The microstructure is considered as one important approach for improved mechanical properties of Ni–Al alloys. Accordingly, there is a great interest in rapid solidification processing of nickel-rich Ni–Al alloys.

Nourbakhsh and Chen [5] prepared Ni–Al alloys containing 61.3–76 at % Ni by the hammer and anvil technique. Their work was focused on the microstructures and mechanical properties of the alloys; however, the microstructure examination by TEM was not very detailed. Cahn *et al.* [6] investigated the order–disorder transition of melt-spun binary alloys containing 75–78 at % Ni as well as ternary alloys. Other authors have studied rapidly solidified alloys containing 65.4 at % Ni [7], 72.7 at % Ni [8], 75 at % Ni [9, 10] and 76 at % Ni [11] separately. Very recently, Lima *et al.* [12] investigated microstructures and mechanical properties of melt-spun Ni–Al–B ribbons containing 68–88.9 at % Ni. However, because of the relatively large ribbon thickness of 200 μm, the cooling rate was only of the order of $3 \times 10^5\,K\,s^{-1}$. Except for melt spinning, very different rapid solidification techniques, including, hammer and anvil techniques and atomization were applied in the other works mentioned. It is well known that there are large differences in cooling rates between these rapid solidification processes. It is difficult to get a consistent view of the effects of composition on metastable microstructures if the published results are compared with each other. Moreover, the discussion of microstructures in most of above-mentioned works rests on a incorrect Ni–Al phase diagram [13], which implies the wrong sequence of eutectic and peritectic reactions as a function of the nickel content near the $Ni_3Al$ phase. Only recently, has an agreement been reached that the eutectic reaction occurs between the β-phase and the γ′-phase, while the γ (Ni)-phase and the γ′-phase involve the peritectic reaction at nickel-rich compositions [1, 14] (see Fig. 1). It is apparent that the effects of high solidification rates on these two reactions may provide a possible way to improve the room-temperature ductility of both γ′ and β intermetallics in addition to other effects related to rapid solidification.

Besides the microstructure control, long-range ordering represents another important feature affecting

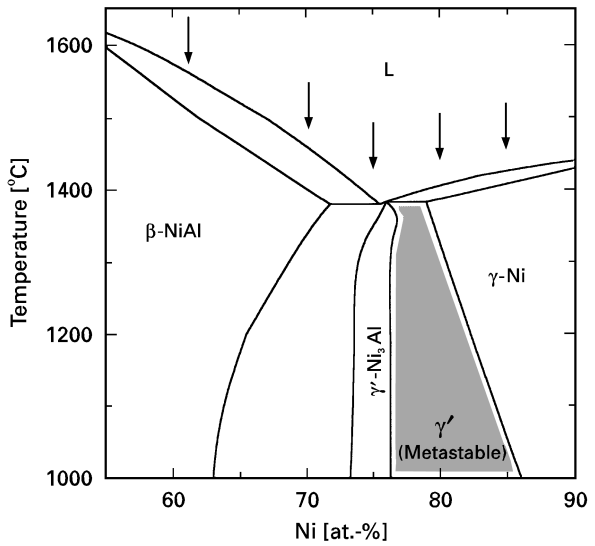


*Figure 1* Reassessed Ni–Al equilibrium phase diagram involving recent corrections of the sequence of the eutectic and the peritectic reaction near to $Ni_3Al$ [1]. The arrows indicate the alloy compositions. Shadded: region of metastable $\gamma'$-ordering.

the room-temperature ductility of intermetallics [6, 15]. It is well known that $Ni_3Al$ maintains the long-range ordered $L1_2$ structure up to its melting point. The ordering energy of the $Ni_3Al$ is quite high and it is very difficult to obtain disordered $Ni_3Al$ even on common rapid solidification. Single-phase disordered f c c $Ni_3Al$ was only achieved by pulsed laser-induced melting of thin films with an interface velocity of about $4\,m\,s^{-1}$ [15]. One important feature of the long-range ordered structure of rapidly solidified $Ni_3Al$-based alloys is the antiphase domains (APD), which represent a possible link with the mechanical properties of $Ni_3Al$ [16]. Employing the dark-field TEM technique combined with selected-area electronic diffraction (SAED) much relevant work on $Ni_3Al$-APDs in rapidly solidified Ni–Al alloys has been accomplished [5, 6, 9–12]. However, there are still quite serious discrepancies between different authors. The complete absence of APDs as well as fine APDs were occasionally reported for the same Ni–Al alloy compositions. Moreover, because most of the mentioned work was concentrated on alloy compositions near the $Ni_3Al$ phase, the effects of nickel content on APD structure and ordering parameter are difficult to assess.

Hence, the effect of composition on microstructures of melt-spun Ni–Al binary alloys covering a wide interval of 61–85 at % Ni has been studied with particular reference to the $Ni_3Al$ APD structure and the degree of ordering. The effects of composition and cooling rate on solidification modes and microstructures are discussed in terms of the reassessed Ni–Al phase diagram (Fig. 1) based on recent solidification experiments [1, 17].

## 2. Experimental procedure

The Ni–Al master alloys with 61, 70, 75, 80, and 85 at % Ni have been prepared from 99.999% pure aluminium and 99.98% pure nickel in a resistance furnace within aluminia crucibles. Alloy portions of 20 g were ejected through a quartz nozzle on to a 300 mm diameter cooper wheel of a melt-spinning facility (rotation rate 500 r.p.m.). The ribbon thickness and width of the melt-spun ribbons were about 40–60 μm and 5 mm, respectively. A cooling rate of the order of $10^6\,K\,s^{-1}$ during rapid solidification was estimated from the ribbon thickness. The composition of melt-spun ribbons was checked by a wet chemical titration method. Deviations from the nominal compositions are less than 0.5 at % Ni. The TEM samples from randomly chosen ribbon sections were prepared in a twin-jet thinning device in a solution of 20 vol% perchloric and 80 vol% acetic acid. Thinning by a single jet from the top surface of the ribbon was employed in order to leave a specimen of the wheel side where the highest cooling rates are expected. Nevertheless, some uncertainty remained about the exact location within a ribbon of the samples investigated by TEM. Alternatively, dimpling with subsequent ion-beam thinning was employed to prepare appropriate thinned areas. No apparent difference between microstructures of the alloy prepared by ion-beam thinning and twin-jet thinning, has been detected. The TEM investigations were performed with a Jeol 200C device. In addition, optical microscopy on ribbon cross-sections and X-ray diffraction (XRD) using Cu$K_\alpha$ radiation have been accomplished.

## 3. Results

### 3.1. Optical microstructure

The optical microstructures change with the composition and local cooling rate differences within the Ni–Al ribbons caused by lateral ribbon–wheel contact fluctuations and the increase of the distance from the chill substrate between the wheel-side and the top-side. For example, at the wheel-side of ribbons containing 70 at % Ni, there are equiaxed grains with martensitic substructure separated by featureless grain-boundary films, as shown in Fig. 2a. With increasing distance from the wheel-side, columnar grains are formed and finally a lamellar eutectic microstructure occurs at the top side. Ribbons containing 85 at % Ni are characterized by extended polygonal grains (see Fig. 2b).

### 3.2. Phase content and TEM microstructure

According to the XRD and SAED analyses, the microstructure of melt-spun ribbons containing 61 at % Ni is relatively uniform and exhibits only polygonal single-phase β-NiAl grains. The average grain size is about 1.5 μm. Different from the predictions of the equilibrium phase diagram (Fig. 1), the precipitation of $Ni_3Al$ ($\gamma'$) phase was completely suppressed on fast cooling and, in addition, the equilibrium phase, $Ni_5Al_3$, did not occur in the as-solidified state in analogy to previous work [7]. A TEM image of a single grain is shown in Fig. 3. The crossed fringes in the grain become visible at a certain tilting angle and represent a special feature of the β-phase called "tweed" structure [18]. Correspondingly, crossed

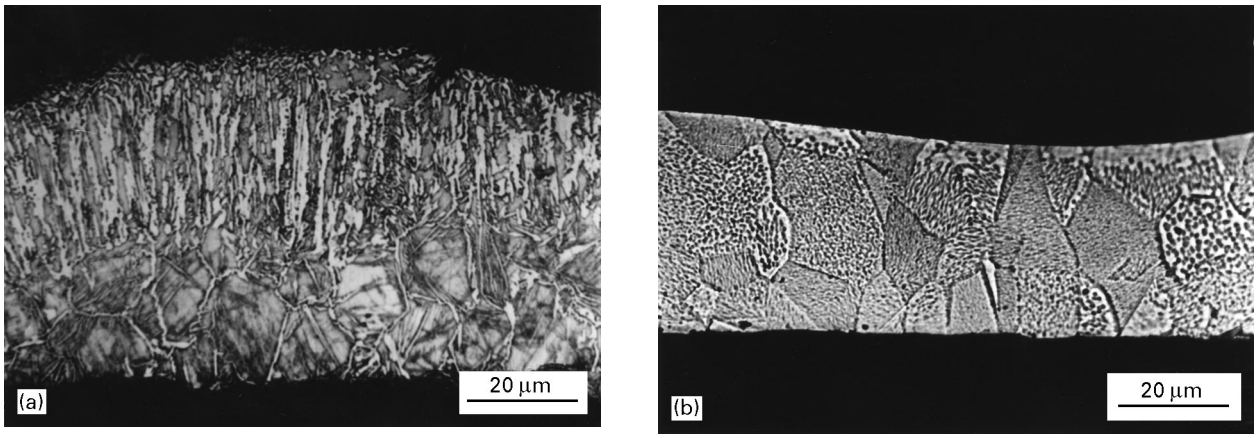


*Figure 2* Cross sectional optical micrographs of a of melt spun Ni–Al alloys containing (a) 70 at % Ni (b) 85 at % Ni.

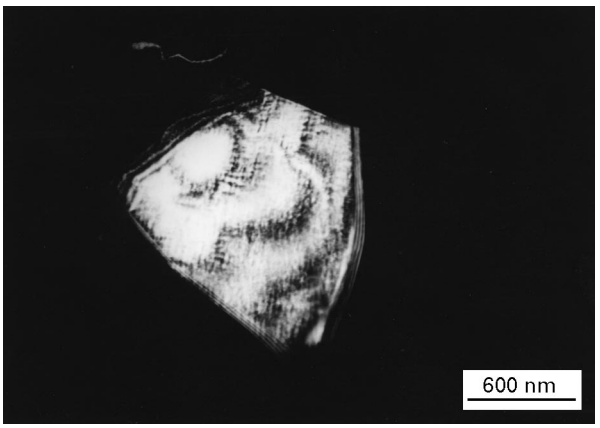


*Figure 3* A β-NiAl grain with 'tweed' structure in melt spun Ni–Al alloy of 61 at % Ni (dark field image).

streaks in each spot of the SAED pattern appear, which are thought to be caused by a kind of planar defect in the β-NiAl phase. Our result can be distinguished from previous work [5, 7] dealing with alloys of slightly higher nickel content, where a transformation into martensitic NiAl (M-NiAl) with a $L1_0$ structure occurs after solidification of the β-NiAl phase. The dislocation density within the β-NiAl grains was very low for this alloy composition, which matches with the brittleness of the ribbon.

Because of different solidification conditions as a function of the distance from the chill surface, illustrated in Fig. 2a, we must expect different TEM microstructures within the 70 at % Ni alloy ribbons. One typical morphology, shown in Fig. 4, consisted of a network of two interpenetrating phases. One phase has a plate-like morphology and exhibits intricate substructures. The average grain size is about 0.8 μm. The analysis of the SAED pattern revealed the $L1_0$ structure of that M-NiAl phase. The substructure of the M-NiAl consists of micro-twins (Fig. 4b, c) or microstacking faults (Fig. 4d). The second phase is the ordered $\gamma'$-$Ni_3Al$ shown in Fig. 5. M-NiAl and $Ni_3Al$ phase interpenetrate each other as shown in Fig. 4a and b. The microstructure resembles the anomalous eutectic morphology favoured by rapid solidification of undercooled eutectic melts [19]. Martensitic grains surrounded by an ordered $\gamma'$-$Ni_3Al$ seam, which was identified by SAED, have also been found (Fig. 5). Comparing Fig. 5 with Fig. 2a we expect this morphology to be preferentially located near the bottom side of the ribbon. On the other hand, Fig. 6a shows a well-developed area of plate-like M-NiAl transformed from β-NiAl grains, which coexists with some internal elongated $Ni_3Al$ grains (Fig. 6b).

The 70 at % Ni alloy ribbon is quite brittle owing to a high volume fraction of the M-NiAl phase. The dislocations appear to be concentrated in the $Ni_3Al$ phase (see Fig. 5) but are absent in M-NiAl. Most of the dislocations in $Ni_3Al$ were associated with the interface between M-NiAl and $Ni_3Al$. Microstructures of the melt-spun 75 at % Ni alloy consist of the major phase and small block-like inclusions distributed either on grain boundaries or within grains of the major phase, which was identified as $Ni_3Al$ by SAED analysis (Fig. 7) and XRD (Fig. 9). The block-like phase M-NiAl was identified by its plate-like morphology (Fig. 8). The observed microstructures match well with previous work concerning alloys of comparable nickel content [5, 8, 10, 12], if one discards differences of the volume fraction of M-NiAl, which presumably depend on the actual cooling rate realized. The average grain size of $Ni_3Al$ is about 1.5 μm and the size of the M-NiAl block is only 60 nm. Most of the $Ni_3Al$ grains show a polygonal pattern although some grain boundaries display a step-like appearance (Fig. 10). The reason for the latter type of grain boundaries is not yet clear. Some twins have been found in $Ni_3Al$, which were also observed in melt-spun Ni–Al alloys with the same composition [5] and are thought to be self-annealed twins. There are many dislocation networks in $Ni_3Al$ grains probably originating from thermal deformation during rapid quenching, interface dislocations between $Ni_3Al$ and M-NiAl blocks, and dislocation pile-ups ahead of the interface, which are indicated in Fig. 7a and c. Accordingly, the ribbon is not very brittle even without boron doping.

The 80 at % Ni ribbons consisted of the ordered $\gamma'$-$Ni_3Al$ phase as proved by the XRD pattern (Fig. 9). The average size of polygonal grains is about 2.5 μm. Apparently, there is a film on the grain boundaries (Fig. 11). In an preceding paper concerning Ni–Al

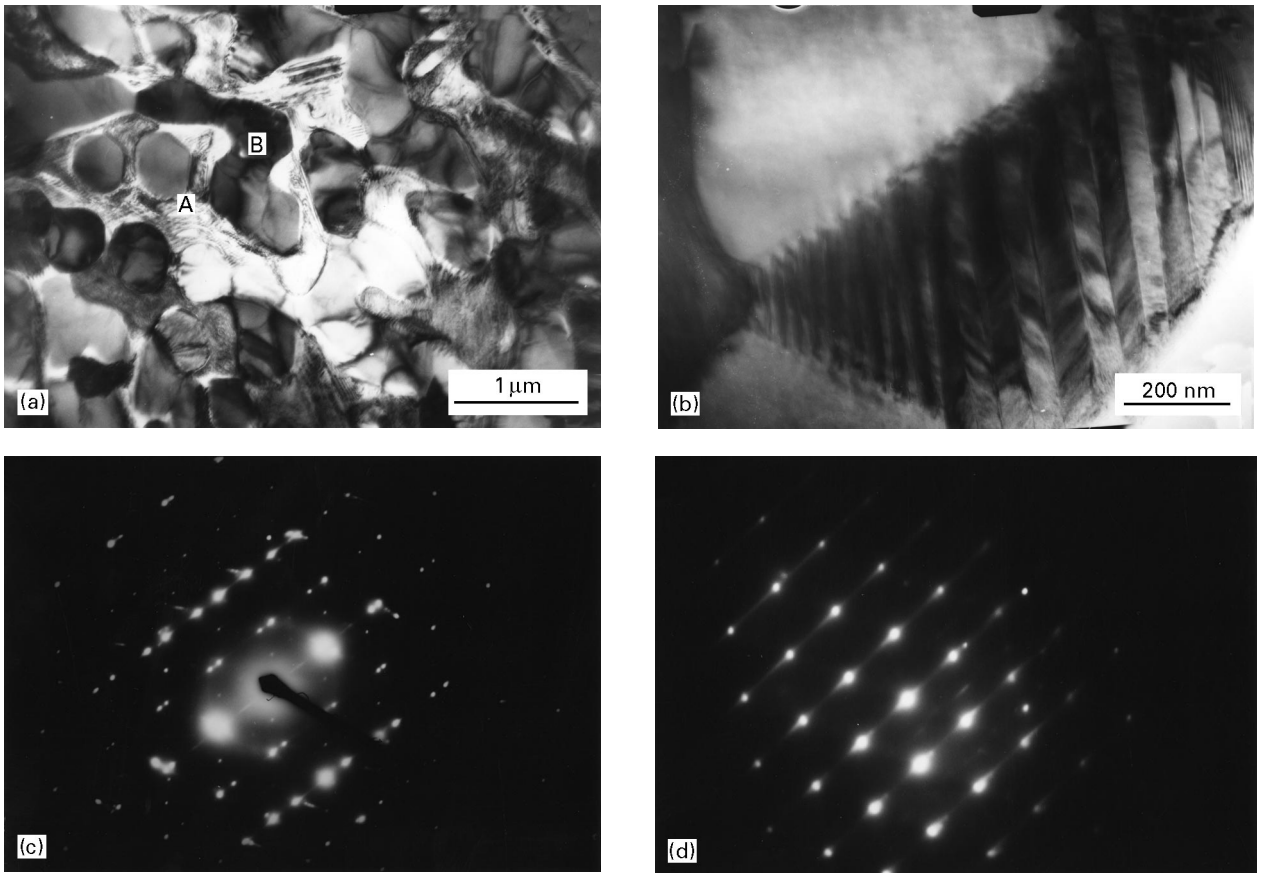


*Figure 4* TEM micrographs of melt spun Ni–Al alloy containing 70 at % Ni (a) coupled growth of (M–NiAl (A) + $Ni_3Al$ (B) two-phase structure (b) M–NiAl with a micro-twin substructure and $Ni_3Al$ (c) SAED pattern of M–NiAl in (b), $L1_0$ [0 2 2] zone (d) SAED pattern of M–NiAl containing a micro-stacking fault substructure, $L1_0$ [0 2 2] zone.

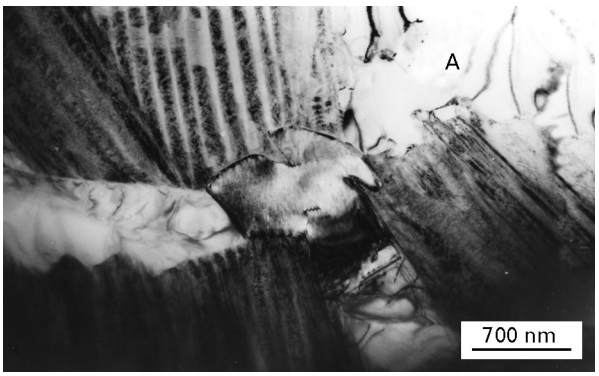


*Figure 5* TEM micrographs of melt spun Ni–Al alloy containing 70 at % Ni. M–NiAl grain surrounded by $Ni_3Al$ grain-boundary phase (A).

droplets with 76.5 at % Ni, such films were claimed to exhibit a disordered γ-Ni structure [10]. However, the carefully tilting, combined with dark-field imaging, revealed that the film exhibits a γ′-$Ni_3Al$ structure, but, as discussed below, the APD sizes differ from the remaining grain. The ductility of ribbons containing 80 at % Ni is reasonably good, despite the lower dislocation density compared with the 75 at % Ni alloy.

The average grain size of 85 at % Ni alloy ribbons is about 5 μm. Many grain boundaries are relatively straight (Fig. 12a). Again step-like grain boundaries occurred in some cases. According to the equilibrium phase diagram (Fig. 1) we expected the γ-Ni disordered solid-solution phase to occur in ribbons containing 85 at % Ni. Much to our surprise, the

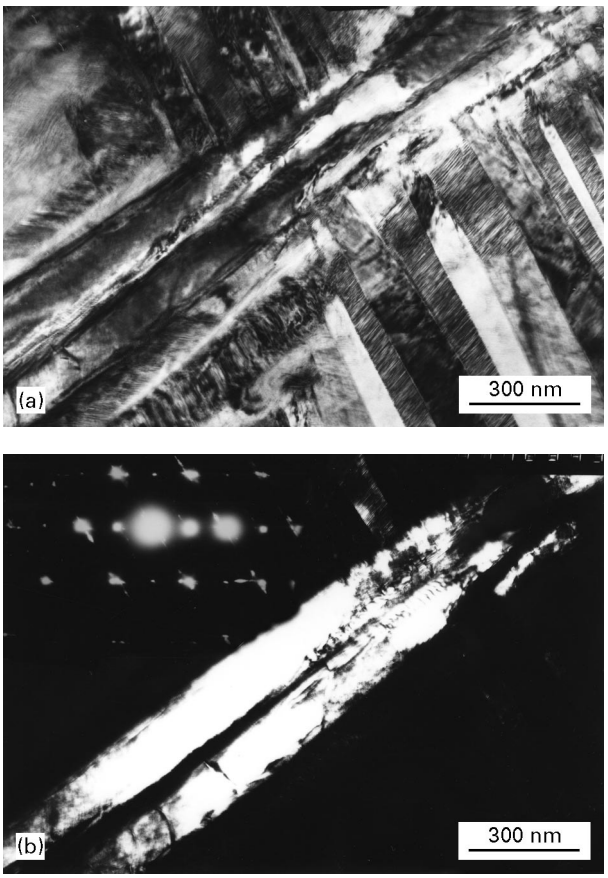


*Figure 6* A well developed M–NiAl with $Ni_3Al$ lamellas in melt spun Ni–Al containing 70 at % Ni (a) TEM micrograph (b) dark field image using $Ni_3Al$ diffraction (insert: SAED pattern of $Ni_3Al$, [001] zone).

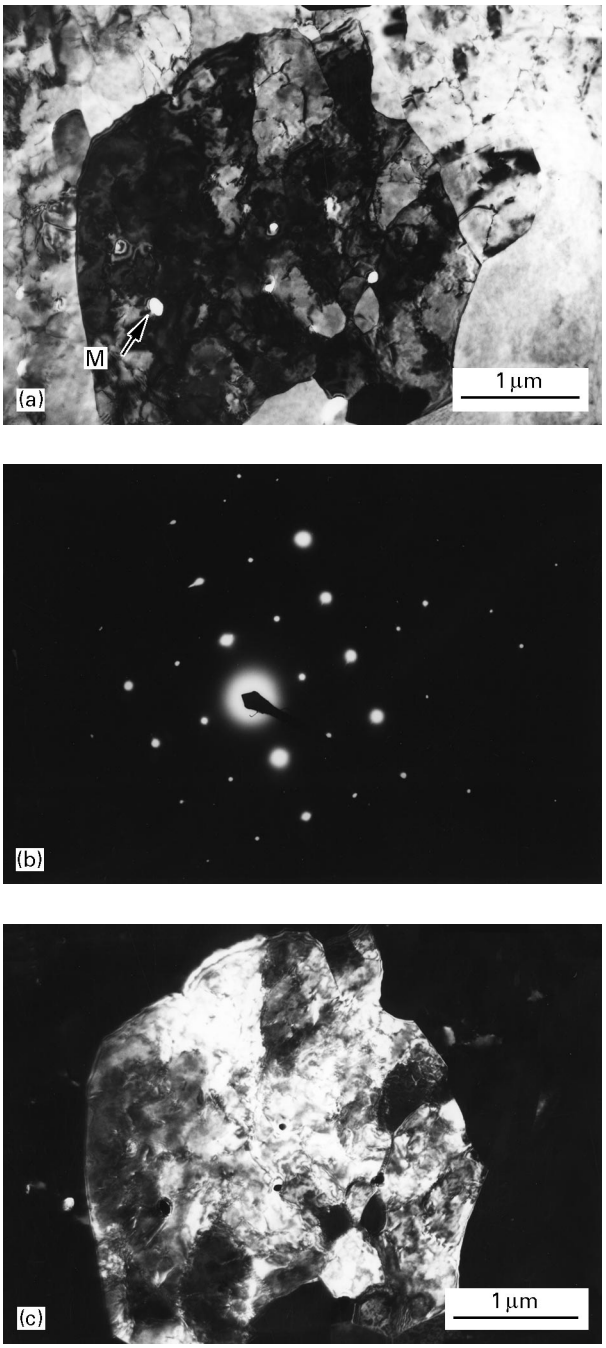


*Figure 7* Microstructures of melt spun Ni–Al containing 75 at % Ni (a) $Ni_3Al$ with small block-like M–NiAl (M) distributed within the grain (b) SAED pattern of $Ni_3Al$, [1 1 2] zone (c) dark field image of the $Ni_3Al$ grain in (a).

microstructure mainly consisted of a single ordered $\gamma'$-$Ni_3Al$ phase. In the XRD analysis (Fig. 9) the appearance of $Ni_3Al$ ordering reflection peaks is very weak. However, the SAED pattern of typical polygonal grain (Fig. 12b) clearly revealed the $L1_2$ ordering reflections of $Ni_3Al$, which were identified in most samples. The relative intensity of ordered spots in the SAED pattern is much weaker than in the 75 and 80 at % Ni ribbons mentioned above. While most of the samples only contain a single $Ni_3Al$ phase, a grain boundary film was detected in a few samples (Fig. 12c). Dark-field imaging with ordered diffraction spots has proved that the film consisted of disordered $\gamma$-Ni phase, different from the similar films in the 80 at % Ni alloy.

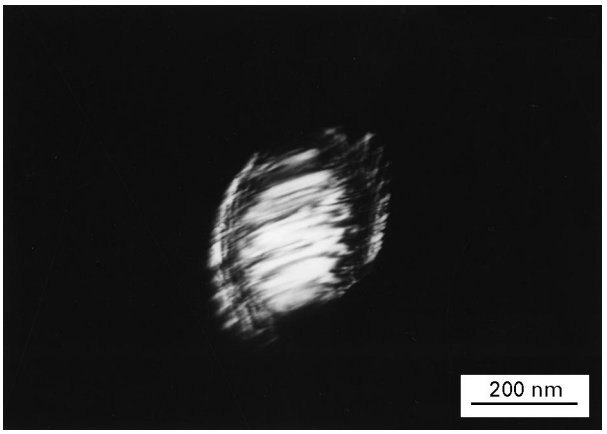


*Figure 8* Plate-like M–NiAl block embedded in a $Ni_3Al$ grain of a melt spun Ni–Al alloy with 75 at % Ni (dark field image).

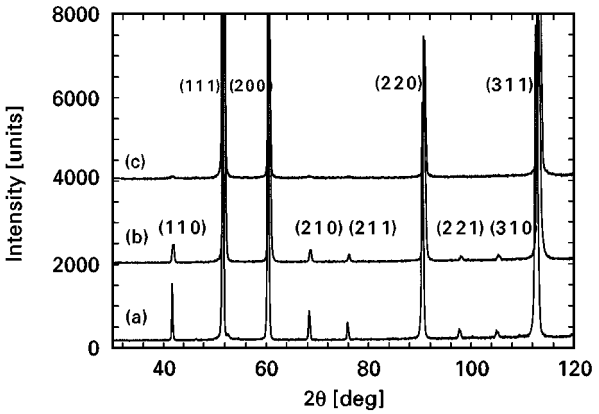


*Figure 9* XRD patterns of melt-spun Ni–Al alloys containing (a) 75 at % Ni, (b) 80 at % Ni and (c) 85 at % Ni ($L1_2$ phase indices are indicated).

### 3.3. $L1_2$ ordering phenomena and $Ni_3Al$-APD pattern

As mentioned in the previous section, the $L1_2$ ordered $\gamma'$-$Ni_3Al$ phase was detected in ribbons containing 70–85 at % Ni. The APD pattern as a function of alloy composition was revealed by a careful examination of SAED patterns and the corresponding dark-field images. A typical $Ni_3Al$ grain in the melt-spun ribbon containing 70 at % Ni is shown in Fig. 13. For that alloy composition, $Ni_3Al$ grains are free of antiphase domain boundaries, indicating direct ordering on freezing. Actually, it is difficult to detect any difference between the dark-field images made from ordered and matrix diffraction spots. The result relates to neither the tilting angle in TEM nor the area in the ribbon, although the feature of APDs normally depends on the appropriate tilting angle in the TEM. Although the $Ni_3Al$ grain shown in Fig. 13 is surrounded by the M-NiAl phase, there is no indication of APD boundary. This suggests a co-operative growth mechanism of $\gamma'$-$Ni_3Al$ + $\beta$-NiAl phases directly from the melt. But, the $\beta$-NiAl transformed into M-NiAl on cooling.

The dark-field image of $Ni_3Al$ grains in ribbons containing 75 at % Ni made from ordered diffraction spots shows that the APD distribution is not homogeneous (Fig. 14). The major part of the grain is

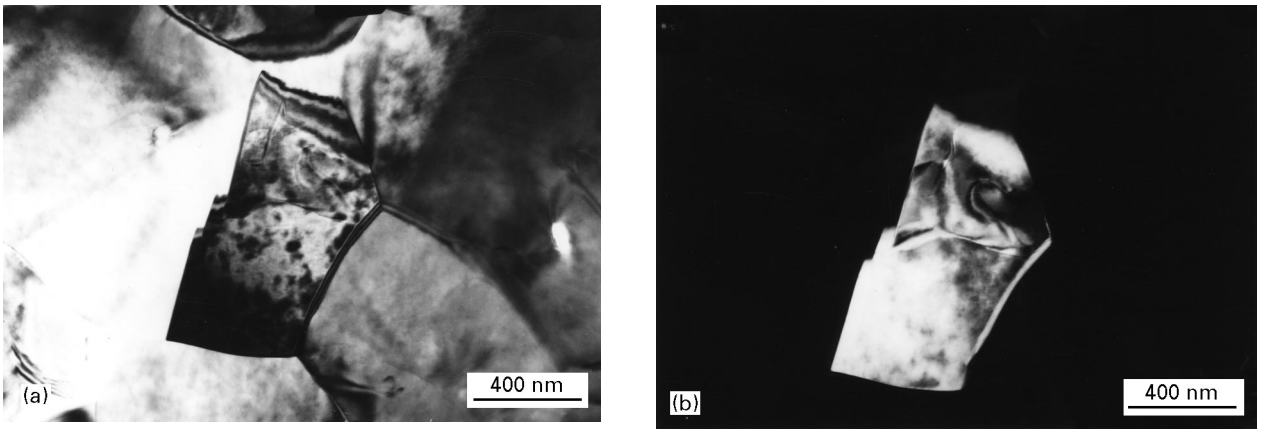


*Figure 10* Polygon-like grains and APDs in $Ni_3Al$ of melt-spun Ni–Al containing 75 at % Ni: (a) bright-field and (b) dark-field using an ordered diffraction.

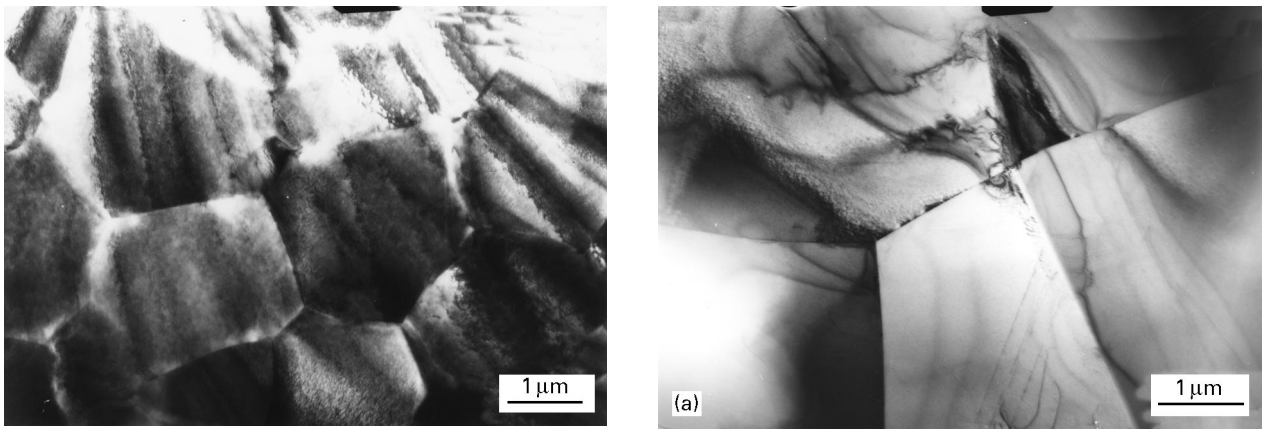


*Figure 11* Microstructures of melt-spun Ni–Al alloy containing 80 at % Ni showing the $Ni_3Al$ grain pattern.

covered by a big single domain of about 0.8 μm size. A few big APDs adjacent to the grain boundaries can be found after carefully tilting. The average size of these APDs is about 0.3 μm. The facts indicate non-homogeneous APD size distribution. A similar feature of APDs in melt-spun alloys of the same composition was shown in a recent paper [16] (compare Fig. 1b of [16]), although the big APD was not indicated and the $Ni_3Al$ grain was classified as devoid of APDs.

Size and distribution of APDs of the 80 at % Ni alloy considerably differ from those of 70 and 75 at % Ni ribbons. Most of the APDs are very fine and homogeneously distributed within the grain (Fig. 15a, c, d). The average size of the fine APDs is about 10–20 nm. The intensity of the ordered diffraction spots in SAED (Fig. 15b) and XRD patterns is much weaker as in the 75 at % Ni alloy. There are a few coarse APDs, which are mainly situated adjacent to grain boundaries. This bimodal distribution of APDs in $Ni_3Al$ was reported in several works dealing with related Ni–Al alloy compositions [5, 6, 9, 11]. Apparently, the visible grain-boundary film discussed in the previous section consists of bigger $\gamma'$-$Ni_3Al$ APD size instead of disordered $\gamma$-phase. This was revealed by carefully tilting the sample combined with numerous dark-field TEM images. We could not find a disordered $\gamma$-film on the fine APDs, which was claimed in

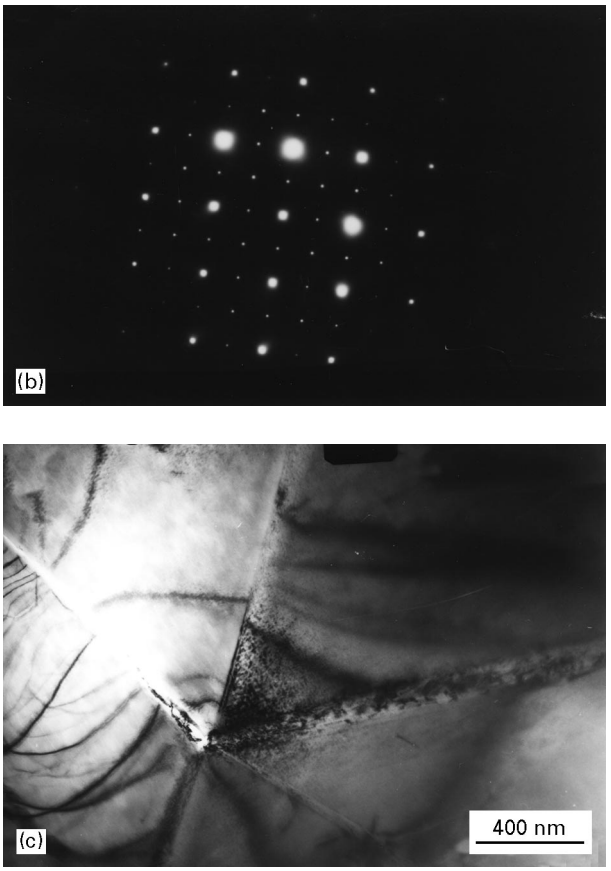


*Figure 12* Microstructures of melt-spun Ni–Al alloy containing 85 at % Ni: (a) grain appearance; (b) SAED pattern, $Ni_3Al$ [0 0 1] zone; (c) bright-field image showing the grain-boundary film.

the work of Cahn *et al.* [6] on melt-spun Ni-22 at % Al alloy. In addition, no structural difference of the boundary between fine APDs and bigger APDs was detected, even at high magnifications.

The dark-field image of $Ni_3Al$ grains in melt-spun Ni–Al ribbons containing 85 at % Ni is unique. In Fig. 16a we observed extremely fine homogeneous distributed zones with an alignment along a preferred direction. The size of the zones could not been determined accurately, but it was estimated to be about 1 nm. The very weak relative intensity of ordered diffraction spots in the SAED demonstrated in Fig. 16b, c matches well with the XRD results. The "antiphase nature" of these zones, termed ordered antiphase zones (APZs), has been confirmed by high-resolution electron microscope dark-field images taken from many different areas and samples. All the results corroborated the existence of those extremely fine

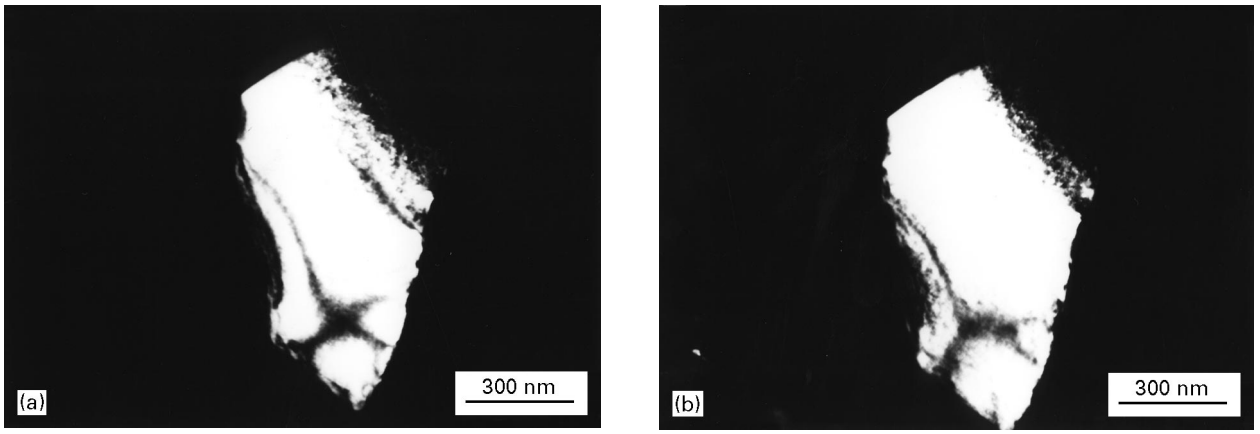


*Figure 13* Dark-field transmission electron micrographs of $Ni_3Al$ grains in melt-spun Ni–Al alloy containing 70 at % Ni to demonstrate the absence of APDs in the ordered phase: (a) matrix diffraction; (b) ordered diffraction.

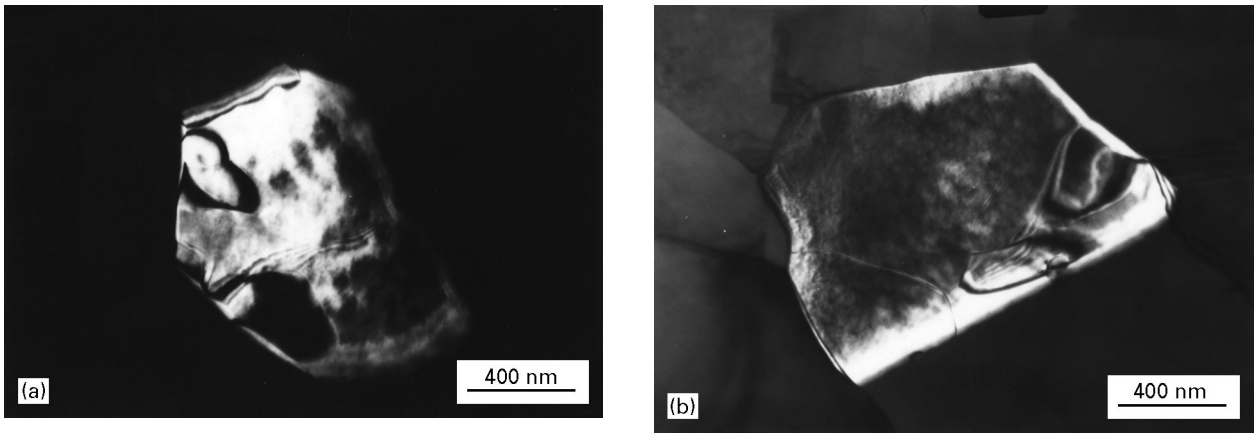


*Figure 14* Dark-field images of two $Ni_3Al$ grains, (a and b), in melt-spun Ni–Al ribbons containing 75 at % Ni, demonstrating the different APD patterns containing a few large APDs.

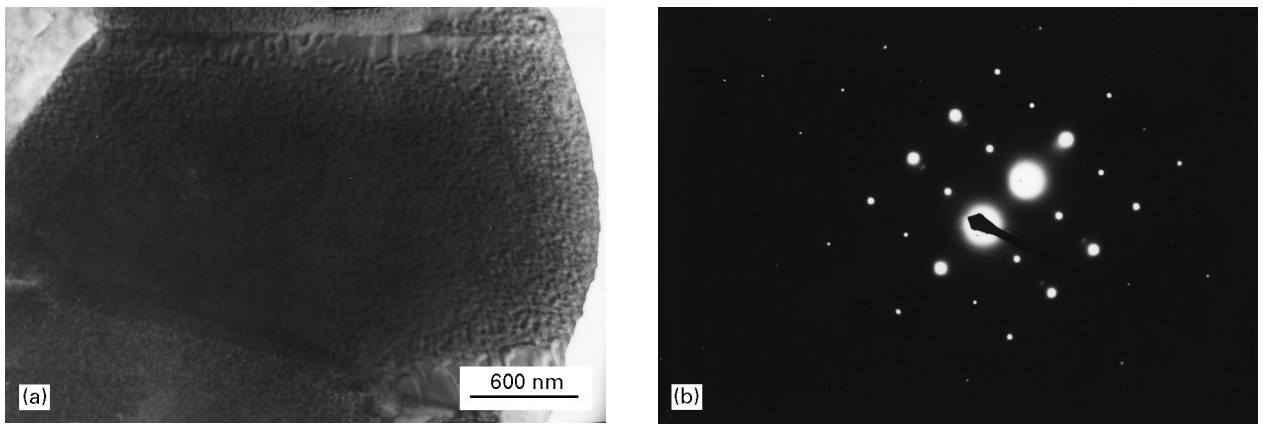


*Figure 15* APDs of $Ni_3Al$ in melt-spun Ni–Al alloy containing 80 at % Ni: (a) $Ni_3Al$ grain (bright-field); (b) SAED pattern, $L1_2$ [1 1 2] zone; (c) dark-field image of the grain shown in (a) using (1 1 0) diffraction; (d) dark-field image of APDs at a high magnification.

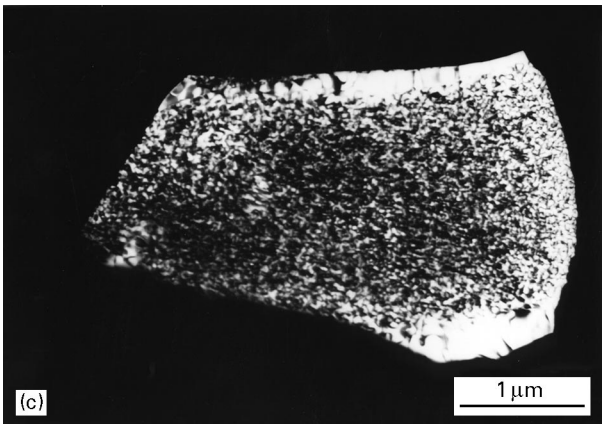


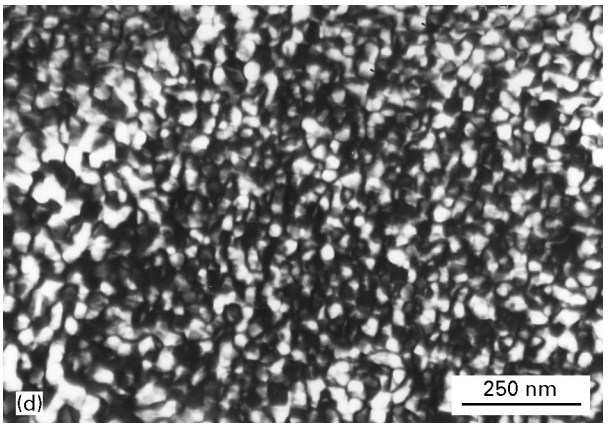


*Figure 15* Continued.

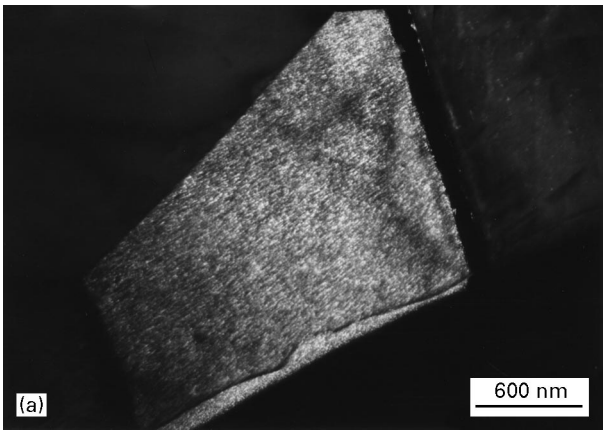


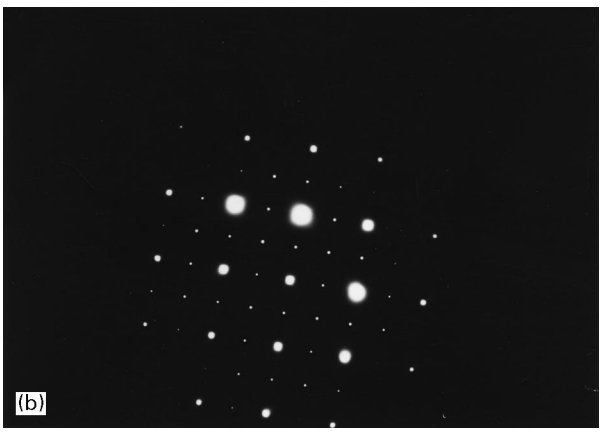



*Figure 16* APDs of $Ni_3Al$ in melt-spun Ni–Al alloy containing 85 at % Ni: (a) dark-field image of a $Ni_3Al$-grain using an ordered diffraction (b); (c) two SAED patterns, $L1_2$ [0 0 1] and [0 1 2] zone, respectively.

ordered zones with low intensity of the ordered diffraction spots described above. To our knowledge this is the first time, that $L1_2$-ordered APZs with very low intensity of ordered diffraction spots have been reported for melt-spun Ni–Al ribbons containing 85 at % Ni.

## 4. Discussion

The microstructures of melt-spun Ni–Al alloys containing 61–85 at % Ni reflected both the influence of composition and a sizeable effect of the high cooling rates of the order of $10^6\,K\,s^{-1}$. With increasing nickel content there is a transition from the β-NiAl to $Ni_3Al$ ordered phase in the as-quenched ribbon. The 61 at % Ni alloy only contained a single ordered β-NiAl phase. The primary β-NiAl solidification mode is apparently preserved for the alloy containing 70 at % Ni. This is concluded from Fig. 2, which displays M-NiAl at the bottom-side of the ribbon. It seemingly originates from the β-NiAl phase, which was transformed on cooling. Owing to the segregation, the residual melt is enriched in nickel until the eutectic composition near 75.5 at % Ni is reached (compare Fig. 1). This causes the solidification of the $Ni_3Al$ featureless seams between the M-NiAl grains in the bottom part of ribbons and can finally lead to the co-operative growth of the β-NiAl (M-NiAl) + $\gamma'$ − $Ni_3Al$ dual-phase microstructure. A direct formation of the $\gamma'$-phase from the melt instead of the disordered γ-phase is presumed because of the absence of APDBs within the $Ni_3Al$ grains. Almost the same M-NiAl + $Ni_3Al$ dual-phase microstructure of melt-spun ribbons has been reported by Nourbakhsh and Chen [5] for Ni–Al alloys containing 69.2–73.8 at % Ni, and Lima and Ferreira [12] for ternary Ni–Al–B alloys containing 71.9 –73 at % Ni. However, referring to the older version of the phase diagram [13] they claimed a separate solidification of $Ni_3Al$ and β–NiAl due to the suppression of the peritectic reaction and postulated a metastable phase diagram involving a β–NiAl + γ–Ni eutectic near 73 at 4% Ni. Apparently, their explanation does not match well with the observed absence of APD in $Ni_3Al$ grains, because for primary γ–Ni growth from the melt and sequential ordering on cooling the resulting $Ni_3Al$ grains were expected to exhibit fine APDs [6].

According to the revised Ni–Al phase diagram the 75 at % Ni alloy investigated is still hypoeutectic. The solidification sequence is difficult to assess solely from the microstructure. From the equilibrium phase diagram (Fig. 1) we infer that solidification starts with β–NiAl before γ′–$Ni_3Al$ can be formed from the melt. However, melt undercooling effects can alter the solidification sequence, too [10, 20, 21]. Assadi *et al.* derived a phase selection diagram of Ni–Al alloys as a function of composition and melt undercooling, $\Delta T$ [21]. It is based on the calculated dendrite growth velocities in undercooled melts. For the near-stoichiometric alloys containing 75 at % Ni, transitions from a preferred growth of the ordered γ′-phase at low undercooling levels, to ordered β–NiAl for $35\,K < \Delta T < 55\,K$, and finally to the disordered γ-phase for $\Delta T > 55\,K$, are predicted. In hyperstoichiometric 76.5 at % Ni alloys the growth of the disordered γ dendrites is preferred for all undercooling levels. Following this line, the observed microstructure in ribbons containing 75 at % Ni, γ′–$Ni_3Al$ grains containing randomly distributed M-NiAl inclusions inside and near grain boundaries, is consistent with moderate undercooling prior to solidification. In that case solidification should start with the β–NiAl phase, which is transformed into M-NiAl on cooling. The subsequent formation of γ′-phase proceeds due to the reduced undercooling level and the nickel segregation in the residual melt. The direct formation of the γ′–$Ni_3Al$ phase from the melt is strongly corroborated by the absence of fine APDs within the grains. Although the directly ordered $Ni_3Al$ grain originates from a single nucleus, any thermal or constitutional perturbation can affect the growth process and severely change the atomic distribution of long-range order. This may result in dislocations or superlattice stacking faults. We conclude that the very few large APDs near to grain boundaries were formed in that way at the end of the grain-growth process. Some dislocations crossing the APDs (see Fig. 14) support this conclusion.

Our results are consistent with those of Cahn *et al.* [6] and Chiba and Hanada [16] who observed almost the same microstructure in Ni–Al ribbons containing 75–76 at % Ni and 74 –75 at % Ni, respectively. The results are also similar to those of Assadi *et al.* [10, 21] for as-solidified undercooled 75 at % Ni samples. However, there are serious discrepancies with some authors who reported a typical bimodal size distribution of $Ni_3Al$–APDs, fine APDs in the centre but coarse APDs near the grain boundaries, in rapidly solidified Ni–Al samples in a similar composition range, notably Nourbakhsh and Chen [5] (75 at % Ni), Cahn *et al.* [6] (77–78 at % Ni), Horton and Liu [9] and Chiba and Hanada [16] (76 at % Ni), and Lima and Ferreira [12] (74.5–78.8 at % Ni). Primarily, we may ascribe this change in microstructure to the slightly higher nickel content of those alloys (compared to 75 at % Ni in our ribbons). This promotes the growth of the disordered γ-phase according to Barth [20] and Assadi *et al.* [21], and fine APDs are formed by sequential ordering on cooling. Segregation effects of nickel-rich alloys lead to nickel depletion of the residual melt and are responsible for the formation of a big APD near grain boundaries [6]. The results of Assadi *et al.* [21] suggest the sensitivity of the microstructure of rapidly solidified Ni–Al alloys near 75 at % Ni to alloy composition fluctuations and melt undercooling. The disordered γ-phase solidification mode is promoted by nickel contents beyond 75 at %, but can also be caused by higher melt undercooling levels prior to solidification [21], which occasionally depend on rapid solidification conditions. Obviously, this hints to the origin of some discrepancies between the results of various authors for identical alloy compositions.

The ribbon containing 80 at % Ni exhibited the $L1_2$ ordered structure. The weaker intensity of the ordered reflections in the SAED and the XRD pattern point to the reduced long-range ordering parameters in comparison with 75 at % Ni alloys. Cahn *et al.* [6] have already shown that the existence range of ordered γ′ can be extended towards metastable nickel-rich compositions. Their experimental results revealed metastable $L1_2$ ordering in rapidly solidified ribbons up to 78 at % Ni. The microstructure of the alloy containing 80 at % Ni is typical for sequential ordering from primarily solidified disordered γ-phase. The fine $L1_2$-ordered APD pattern agrees with similar features from previous work [9, 10, 12, 15, 16]. Segregation during γ-solidification leads to a gradual aluminium-enrichment of the residual melt [9], which can promote the direct γ′-phase solidification of the final part. Accordingly, the visible film near grain boundaries consists of coarse inhomogeneously distributed γ′–$Ni_3Al$ APDs, which had directly solidified from melt. The peritectic reaction in the equilibrium phase diagram was seemingly suppressed in the melt-spun ribbons containing 80 at % Ni because there was no trace of γ-film on grain boundaries, which would typically arise in this growth mechanism. Our results on 85 at % Ni alloys suggest metastable $L1_2$-ordering due to high cooling rates of the order of $10^6\,K\,s^{-1}$ at the highest nickel-content so far reported. The relative intensities of ordered reflections in SAED patterns are rather weak indicating a low degree of long-range order. Some disordered γ-films on grain boundaries were detected in a few grains notably near to the top of the ribbon. Lima and Ferreira [12] only observed the disordered γ-phase in about 200 μm thick ribbons containing 82–88.9 at % Ni. This important difference may be due to the slower cooling rate of about $3 \times 10^5\,K\,s^{-1}$ corresponding to that ribbon thickness. The nature of this metastable γ′-phase is still obscure. The order parameter is again much reduced in comparison with the 80 at % Ni ribbon. Following Cahn *et al.* [6], this ordered metastable phase can only be formed if the nucleation of the ordered equilibrium phase is circumvented until the existence range of the metastable phase (slightly below the γ–Ni solvus line) is reached. Extrapolating Cahn *et al.*'s results to 85 at % Ni, we infer that the metastable $L1_2$ ordering should only proceed below 1100 °C. This low ordering temperature matches with the extremely fine APZ size of 1 nm.

A change from complete disorder to short-range order and finally to long-range order was revealed in

an irradiated Cu–Pb solid solution at different temperatures [22]. The modulated short range order exhibited weak ordered diffraction spots in SAED patterns in high-voltage electron microscopy. The additional spots were ascribed to spinodal ordering. Because, in the present case, the APZs in the 85 at % Ni alloy can be directly observed in TEM images, this kind of weak long-range order is expected to be somewhere between a common long-range ordering and the spinodal ordering.

## 5. Conclusions

1. The microstructure investigations of melt-spun Ni–Al ribbons containing 61–85 at % Ni revealed the transition from primary β–NiAl (61, 70, 75 at % Ni) to disordered γ-phase solidification (80, 85 at % Ni) with increasing nickel content of the alloys.

2. The effects of off-stoichiometry on the $L1_2$ ordering appear different at the aluminium-rich and nickel-rich sides, respectively. For hypostoichiometric and stoichiometric alloys (70, 75 at % Ni) there is a direct formation of the $Ni_3Al$-phase from the melt (preceded by the primary β–NiAl solidification). This is indicated by large APD size (or the absence of APDBs) and severe long-range ordering. Hyperstoichiometric (80 and 85 at % Ni) alloy ribbons exhibit a metastable $L1_2$-ordered structure with fine APD patterns and weak intensity of ordered spots, which formed by sequential ordering on cooling.

3. Although segregation is normally not severe in rapidly solidified alloys, it seemingly affects the microstructure of Ni–Al ribbons. In hypoeutectic 70 at % Ni alloys the gradual change from M-NiAl grains at the bottom side to a M-NiAl + $Ni_3Al$ dual-phase microstructure is due to the nickel macrosegregation during β-NiAl solidification. This shifts the residual melt composition toward the eutectic composition. Microsegregation in hyperstoichiometric alloys leads to an aluminium enrichment around the growing grains, which is the origin of the large APDs near the grain boundaries.

4. Besides the alloy composition, the melt undercooling prior to solidification represents a second important factor affecting the solidification mode. There is some evidence that the different microstructures of rapidly solidified samples near 75 at % Ni result from occasional scatter in solidification conditions.

5. One of the important findings was the metastable $L1_2$ ordering of ribbons up to 85 at % Ni. This is far beyond the hitherto reported limits. The features and formation mechanisms of those metastables ordered structures will be a subject of future work.


## Acknowledgements

Tianyi Cheng was visiting scientist at the IFW Dresden and thanks, Professor L. Schultz for his invitation. The authors thank Mrs M. Reibold and Dr H.-D. Bauer for their kind support in TEM activities, Mrs I. Stange for X-ray diffraction experiments, Professor L. Schultz useful discussions, and Dr M. Barth providing his melt undercooling results prior to publication.


## References


1. J. H. LEE and J. D. VERHOEVEN, *J. Phase Equilib.* **15** (1994) 136.
2. R. D. NOEBE, R. R. BOWMAN and M. V. NATHAL, *Int. Mater. Rev.* **38** (1993) 193.
3. C. T. LIU, *Scripta Metall.* **25** (1991) 1231.
4. S. C. DEEVI and V. K. SIKKA, *Intermetallics* **4** (1996) 357.
5. S. NOURBAKHSH and P. CHEN, *Acta Metall.* **37** (1989) 1573.
6. R. W. CAHN, P. A. SIEMERS, J. E. GEIGER and P. BARDHAN, *ibid.* **35** (1987) 2737.
7. TIANYI CHENG, *Scripta Metall. Mater.* **27** (1992) 771.
8. TIANYI CHENG and SHOUHUA ZHANG, *J. Mater. Sci. Lett.* **9** (1990) 953.
9. J. A. HORTON and C. T. LIU, *Acta Metall.* **33** (1985) 2191.
10. H. ASSADI, M. BARTH, A. L. GREER, D. M. HERLACH and P. ADEVA, in "Materials Science Forum", vol. 179–181 (Trans Tech Publications, Switzerland, 1995) p. 741.
11. C. C. KOCH, J. A. HORTON, C. T. LIU, O. B. CAVIN and J. O. SCARBROUGH, in "Proceedings of the Third Conference on Rapid Solidification Processing", edited by R. Mehrabian (National Bureau of Standards, Washington, DC, 1982) p. 264.
12. M. S. LIMA and P. I. FERREIRA, *Intermetallics* **4** (1996) 85.
13. M. F. SINGLETON, J. L. MURRY and P. NASH, in "*Binary Alloy Phase Diagrams*", edited by T. B. Massalski, (American Society for Metals, Metals Park, OH, 1986) p. 140.
14. R. D. NOEBE, A. MISRA and R. GIBLA, *ISIJ Int.* **31** (1991) 1172.
15. J. A. WEST and M. J. AZIZ, in "Kinetics of Ordering Transformations in Metals", edited by H. Chen and V. K. Vasudevan (TMS, Warrendale, PA, 1992) p. 59.
16. A. CHIBA and S. HANADA, *Intermetallics* **4** (1996) 55.
17. J. H. LEE and J. D. VERHOEVEN, *J. Crystal Growth* **142** (1994) 193.
18. S. M. SHAPIRO, J. Z. LARSEN, Y. NODA, S. C. MOSS and L. E. TANNER, *Phys. Rev.* **B57** (1986) 3199.
19. B. WEI, D. M. HERLACH, F. SOMMER and W. KURZ, *Mater. Sci. Eng.* **A173** (1993) 355.
20. M. BARTH, PhD thesis, Ruhr-Universität Bochum (1995).
21. H. ASSADI, M. BARTH, A. L. GREER and D. M. HERLACH, *Acta Mater.* **46** (1998) 491.
22. S. TAKEDA, J. KULIK and D. de FONTAINE, *Acta Metall.* **35** (1987) 2243.



*Received 13 November 1997*
*and accepted 15 May 1998*